

Contents lists available at ScienceDirect

Mechanical Systems and Signal Processing





New inverse wavelet transform method with broad application in dynamics



Alireza Mojahed a,*, Lawrence A. Bergman b, Alexander F. Vakakis a

- ^a Department of Mechanical Science and Engineering, University of Illinois, Urbana, IL 61801, United States
- ^b Department of Aerospace Engineering, University of Illinois, Urbana, IL 61801, United States

ARTICLE INFO

Article history: Received 7 July 2020 Received in revised form 19 January 2021 Accepted 23 January 2021

Keywords: Inverse wavelet transform Harmonic decomposition System identification Geometric nonlinearity

ABSTRACT

Extracting multi-scale models from system identification of stationary or nonstationary measured signals (e.g., time series) is of great importance in engineering and the applied sciences. We propose a new computational method for harmonic analysis and decomposition of signals based on the inverse wavelet transform and demonstrate its efficacy in diverse areas in dynamics. The wavelet transform is a linear transformation of a signal measured in the temporal/spatial domain to the time-frequency/space-wavenumber domain and applies to stationary and nonstationary measurements. The new method is based on a numerical inverse wavelet transform and yields decomposition of the measured signal in terms of its dominant harmonic components. First, we formulate the analytical continuous inverse wavelet transform in a way that is suitable for computational implementation. Then, taking as example a general measured signal in the time domain, (i) we numerically compute its numerical wavelet transform spectrum, (ii) define a set of "harmonic regions" in the wavelet spectrum containing the dominant harmonics to be inverted and studied, and (iii) by numerically inverse wavelet transforming each of the harmonic regions separately, obtain the respective decomposed harmonics in the time domain. Note that, by construction, the superposition of all decomposed harmonics reconstructs the original signal. Next, we demonstrate the efficacy of the method with some examples. We start with an artificial signal with prescribed harmonic components to highlight the method and its accuracy. Then, we show applicability of the method to system identification, by applying it to the modal analysis of a system of linearly coupled oscillators with closely spaced modes. Lastly, we show how the new method enables quantification of the energy captured by each of the decomposed components (harmonics) in the response of a strongly nonlinear system. To this end, a single degree of freedom geometrically nonlinear oscillator is considered, and the method is used to quantify nonlinear energy "scattering" in its frequency domain. These examples hint at the broad applicability of the new method to diverse areas of signal processing and dynamics, including discrete and continuous dynamical systems with strongly (and even non-smooth) nonlinearities.

© 2021 Elsevier Ltd. All rights reserved.

1. Introduction

In studying dynamical systems, it is often crucial to identify and study the different time-scales that govern their responses. To this end, system identification addresses the issue of constructing mathematical reduced-order models for

^{*} Corresponding author.

dynamical systems by analyzing their measured responses [1]. System identification typically relies on post-processing measured data either in the frequency domain, e.g., Fourier transforms, or in the time–frequency domain, e.g., short-time Fourier and wavelet transforms.

One of the widely used time-frequency analysis techniques is the Empirical Mode Decomposition (EMD) [2], which is a data-driven technique that decomposes measured signals into independent oscillatory wave-functions, termed Intrinsic Mode Functions (IMFs). Unfortunately, often the identified IMFs are not entirely monochromatic, capturing more than a single time (frequency) scale of the signal; this important limitation of EMD is referred to as mode mixing. Mode (or scale) mixing occurs, e.g., when the measured signal possesses closely spaced frequency components; this typically happens when $0.5 < \omega_i/\omega_i < 2$, where ω_i and ω_i are two closely spaced frequency scales contained in the signal [3]. Another case resulting in mode mixing is when the amplitude ratio of two IMFs is either very large or very small. Accordingly, several modifications have been proposed to EMD to address the mode mixing issue. Kurt et al. obtained accurate EMD decomposition by manually applying and optimizing masking signals in the measured response [4–7], successfully decomposing one IMF component at a time. Building on this concept, Moore et al. introduced the wavelet-bounded empirical mode decomposition (WBEMD) [8,9], which relies on the use of wavelet transforms to optimize the "separation" of an IMF around a characteristic frequency scale to yield well-separated (in scale) IMFs. In another study, Qin et al. introduced a modal analysis technique based only on output measurement, by employing an improved version of EMD to avoid mode mixing [10]. Lastly, Sadhu combined multi-variate with ensemble EMD to overcome mode mixing and compute scaleindependent IMFs [11]. Apart from posing limitations in EMD, the problem of mixed scales (i.e., of non-separable, closely spaced scales) is a far more general issue in engineering and the applied sciences, as it is often related to highly nonstationary phenomena and increased complexity in the measured outputs. This is a common occurrence, e.g., at points of bifurcation, in sudden dynamical transitions, or during break of synchronicity, adding new scales in the responses due to the governing physics.

Issues such as scale mixing highlight the need for developing robust methods to perform effective harmonic decomposition of measured highly non-stationary signals, where current techniques are not effective. Accordingly, in this work we propose a new method for accurate harmonic decomposition of measured signals based on the inverse wavelet transform. The wavelet transform, similar to the short-time Fourier transform [12–14], is a method of transforming a signal from the temporal/spatial domain to the time–frequency/space-wavenumber domain. This enables direct study of the temporal/spatial evolutions of the dominant harmonic components (scales) contained in the measured signal. Moreover, due to its mathematical closed-form formulation, the wavelet transform is convenient in its implementation even for signals where mixed scales are present [15]. These observations provide ample motivation for the proposed method, which relies on numerical inverse wavelet transforms, and is applicable to the analysis of even complex and nonstationary signals that are encountered in diverse applications in dynamics.

Wavelet transform – in both continuous and discrete forms – has been used as a means to perform modal separation and system identification. For instance, Boltežar and Janko [16] proposed different methods to rectify numerical "boundary effects" when computing the continuous wavelet transform for damping identification in measured signals. This work focuses on linear and lightly damped mechanical systems with proportional damping. Huang and Su [17] and Wang et al. [18], also employed continuous wavelet transforms for system identification of linear time-invariant systems. Their methodology was developed solely to accommodate linear dynamical systems. Employing the wavelet transform, Quqa et al. presented a decentralized procedure for nearly real-time modal identification. Through a modal assurance criterion (MAC)-based clustered filter bank (CFB) they were able to determine time-varying natural frequencies and mode shapes of dynamical systems which then used for damage diagnosis [19] In another study, they further developed their methodology to perform robust modal identification for dynamical systems that is robust to narrow-band disturbances and white noise, and is applicable to systems with vanishing modes [20].

In this paper, we propose a harmonic (mode) decomposition technique based on the continuous wavelet transform. Apart from being a harmonic decomposition technique which can be applicable to multi-harmonic signals, e.g., response of dynamical systems, sound signals, etc., the proposed technique can be used in the form of a purely data-driven system identification methodology. In what follows, we begin by discussing the continuous wavelet transform (CWT), the inverse continuous wavelet transform (ICWT), efficient computation techniques for CWT and ICWT, and the basic aspects of the proposed method. Next, we apply the method to a signal with two time-varying frequency components, in order to examine if mode mixing can be addressed by our approach. Moreover, we compare the separated harmonics from this example to those obtained by an EMD-based method. Next, we study a three degree-of-freedom (DOF) system of linear coupled oscillators and demonstrate the applicability of the ICWT-based method for system identification of a linear system with closely spaced and vanishing modes. Lastly, we switch to a nonlinear application by studying the free response of a single-DOF, geometrically nonlinear oscillator [21–23] in two different configurations: One yielding hardening stiffness nonlinearity, and the other a combination of hardening and softening stiffness nonlinearity. For this system we show that the proposed method can be used to quantify the energy scattering in the frequency domain that is caused by the geometric nonlinearity. We end with a synopsis of the main findings of this work and a discussion of its applicability to a broad class of dynamical systems.

2. Background and ICWT-based harmonic decomposition method

2.1. Continuous wavelet transform (CWT)

The CWT is a method of transforming a signal from the temporal/spatial domain, to the time–frequency/space-wavenum ber domain, revealing important features that are not readily available, e.g., by the Fourier transform. Considering a signal in the time domain, x(t), its CWT is defined by the following general expression,

$$X(a,b) = \frac{1}{\sqrt{a}} \int_{-\infty}^{\infty} x(s)\overline{\psi}\left(\frac{s-b}{a}\right) ds \tag{1a}$$

$$X(\omega,t) = \sqrt{\frac{\omega}{\omega_c}} \int_{-\infty}^{\infty} x(s)\overline{\psi} \left(\omega \frac{s-t}{\omega_c}\right) ds \tag{1b}$$

where the *wavelet* $\psi(t)$ is a complex function that is localized in the time and frequency, b represents time and a is the so-called "dilation parameter" of the wavelet. In order to relate the dilation parameter a, to frequency, ω , it is replaced by $a = \omega_c/\omega$ – cf. Eq. (1b). Additionally, overbar denotes complex conjugate, and ω_c , the center frequency of the wavelet, is defined by,

$$\omega_c = \sqrt{\frac{\int_0^\infty \omega^2 |\Psi(\omega)|^2 d\omega}{\int_0^\infty |\Psi(\omega)|^2 d\omega}}$$
 (2)

where $\Psi(\omega) = \int_{-\infty}^{\infty} \psi(t) \exp{(-i\omega t)} dt$ denotes the Fourier transform of $\psi(t)$, $i = \sqrt{-1}$, and $|\cdot|$ the magnitude of its argument. Note that the wavelet $\psi(t)$ defines the specific wavelet family considered and is not unique in its definition. In scenarios where computing the Fourier transform of a signal is not possible, implementing fast Fourier transform (FFT) is more suitable. In such scenarios, there are several practical issues that need to be considered though, such as zero-padding the signal, x(t), to ensure that the number of samples of x(t) is a power of 2. Additionally, it is preferred that x(t) is sampled uniformly, and, to obtain a meaningful wavelet transform in the frequency domain, the sampling frequency of the signal must be at least twice the maximum frequency that is to be studied by the wavelet transform.

For a function $\psi(t)$ to be classified as a wavelet it should possess certain properties. Namely, it should possess finite "signal energy,"

$$I = \int_{-\infty}^{\infty} |\psi(t)|^2 dt < \infty \tag{3}$$

and zero mean (admissibility condition):

$$C = \int_0^\infty \frac{|\Psi(\omega)|^2}{\omega} d\omega < \infty \tag{4}$$

Moreover, for complex wavelets, such as the Morlet wavelet [15], it must hold that:

$$\lim_{\omega \to -\infty} \text{Re}\{\Psi(\omega)\} = 0, \text{Im}\{\Psi(\omega)\} = 0 \tag{5}$$

The Morlet wavelet is a complex wavelet capable of separating the phase and the amplitude of the harmonic components within a signal and is defined as:

$$\psi(t) = \pi^{-1/4} \left(e^{i\omega_c t} - e^{-\omega_c^2/2} \right) e^{-t^2/2} \tag{6}$$

Accordingly, based on (1b), the Morlet CWT of the signal x(t) is expressed as:

$$X(\omega,t) = \sqrt{\frac{\omega}{\pi^{1/2}\omega_c}} \int_{-\infty}^{\infty} x(s) \left[e^{-i\omega(s-t)} - e^{-\omega_c^2/2} \right] e^{-\left(\omega\frac{s-t}{\omega_c}\right)^2/2} ds \tag{7}$$

Relation (7) is the exact analytical expression of the CWT of signal x(t), but it is computationally expensive when discretized in practical applications, especially when dealing with large datasets. To remedy this issue, we refer to (1b) and recognize that $X(\omega,t)$ is expressed as the convolution of two functions, namely, x(t) and $\psi(\omega t/\omega_c)$; therefore, by applying Parseval's theorem to (1b), we express $X(\omega,t)$ as,

$$X(\omega,t) = \sqrt{\frac{\omega_c}{\omega}} \int_{-\infty}^{\infty} \widetilde{X}(\xi) \, \bar{\Psi}(\xi \omega/\omega_c) e^{i\xi t} d\xi \tag{8}$$

Relation (8) is an efficient representation of the wavelet transform in practice, since it incorporates the Fourier transform – which translates to the numerical fast Fourier transform (FFT) in practice, and consequently, leads to significant speedup in computing the wavelet transform of a signal. However, as stated earlier special care regarding the sampling rate, number of samples, etc. must be taken to ensure meaningful outputs.

2.2. Inverse continuous wavelet transform (ICWT) and proposed method

Now for the same signal, x(t), with wavelet transform, $X(\omega, t)$, given by (1b) or (8), the ICWT of $X(\omega, t)$ – which recovers x(t), is computed by:

$$x(t) = -\frac{1}{\omega_c C} \int_0^\infty \int_{-\infty}^\infty X(\omega, s) \sqrt{\frac{\omega}{\omega_c}} \psi\left(\omega \frac{t - s}{\omega_c}\right) ds d\omega \tag{9}$$

Similar to (1b), the exact expression of the ICWT, (9), is computationally inefficient. Therefore, to be able to employ the FFT and inverse Fourier transform (IFFT) techniques and improve the efficiency of the ICWT, we apply again Parseval's theorem to (9) and obtain,

$$x(t) = \frac{1}{\omega_c C} \int_{0}^{\infty} \sqrt{\frac{\omega_c}{\omega}} \int_{-\infty}^{\infty} \widetilde{X}(\omega, \xi) \Psi(\xi \omega/\omega_c) e^{i\xi t} d\xi d\omega$$
 (10)

where $X(\omega,\xi)$ is the Fourier transform of $X(\omega,t)$ with respect to its second argument, t. Similar to (8), (10) is now in a form that is amenable to direct application of the FFT and IFFT, so it is computationally efficient.

In the practical implementation of the ICWT (such as the applications discussed in the next sections), one can express $X(\omega,t)$ in the following series form,

$$X(\omega,t) = \sum_{i=1}^{N} X_j(\omega,t)$$
 (11)

where $X_j(\omega,t)$ is the j-th "harmonic region" in the time–frequency plane of the CWT spectrum $X(\omega,t)$, and is expressed explicitly as,

$$X_{i}(\omega, t) = X(\omega, t) \{ H[\omega - \omega_{i-1}(t)] - H[\omega - \omega_{i}(t)] \}, \omega_{i-1}(t) < \omega_{i}(t)$$

$$(12)$$

where $\omega_0 = 0$, $\omega_N \to \infty$, and H(.) represents the Heaviside function. Note that, geometrically, the harmonic regions (12) correspond to non-uniform "strips" in the frequency-time plane, with each capturing a separate harmonic of the CWT. Moreover, in practical applications, ω_N at most can be equal to the Nyquist frequency of the discretized signal. Substituting (11) and (12) into (9), we obtain the recovered signal from the ICWT in terms of a superposition of N harmonics $x_i(t)$,

$$x(t) = \sum_{j=1}^{N} x_j(t)$$
 (13)

where,

$$x_{j}(t) = -\frac{1}{\omega_{c}C} \int_{0}^{\infty} \int_{-\infty}^{\infty} X_{j}(\omega, s) \sqrt{\frac{\omega}{\omega_{c}}} \psi\left(\omega \frac{t-s}{\omega_{c}}\right) ds d\omega = \frac{1}{\omega_{c}C} \int_{0}^{\infty} \sqrt{\frac{\omega_{c}}{\omega}} \int_{-\infty}^{\infty} \widetilde{X}_{j}(\omega, \xi) \Psi\left(\frac{\xi\omega}{\omega_{c}}\right) e^{i\xi t} d\xi d\omega$$
 (14)

and $X_j(\omega,\xi)$ is the Fourier transform of $X_j(\omega,t)$ with respect to its second argument, t. With proper choice of the harmonic regions in the frequency-time plane, $x_j(t)$ represents the j-th decomposed harmonic of x(t).

Expression (13) yields a harmonic decomposition of the signal x(t) in terms of its dominant harmonics. The distinct beneficial feature of this method is its versatility and flexibility in its application, as the user can select manually the harmonic regions that need to be inverted in the frequency-time domain; given that the CWT provides detailed information on the evolution of the dominant harmonics of the measured signal in time or space, the user can select and separate the different harmonics based on a number of criteria, and invert them one by one to obtain a very effective harmonic decomposition of the signal. This feature makes the method applicable to diverse applications in dynamics, including stationary or nonstationary measurements, linear or nonlinear responses and signals with separated scales or mode mixing.

3. Numerical examples and applications

To demonstrate the method of application and capacity of the proposed harmonic decomposition method, we now apply it to three different applications. Starting from the decomposition of an artificial nonstationary signal, we proceed to apply the method to modal analysis of a three DOF linear system of coupled oscillators with two closely spaced modes (i.e., mode

mixing). Lastly, we implement the method to a geometrically nonlinear single-DOF oscillator to show how the proposed method can provide a quantification of nonlinear energy scattering in the frequency domain of the system dynamics.

3.1. Artificial signal - Method verification

We start by considering the following artificial signal composed of stationary and nonstationary (with time-varying frequency) components and use non-dimensional units for convenience,

$$y(t) = y_1(t) + y_2(t) = \frac{1}{4}e^{-0.05t}\sin\phi_1(t) + e^{-0.05t}\cos\phi_2(t) \tag{15}$$

where.

$$\phi_1(t) = \int_0^t \Omega_1(s) ds = \int_0^t \left(1 + 4e^{-0.025s}\right) ds \tag{16a}$$

and

$$\phi_2(t) = \int_0^t \Omega_2(s) ds = \int_0^t \{5 + 2[[H(s) - H(s - t_0)] \cos(\pi s/t_0) - H(s - t_0)]\} ds$$
(16b)

where $t_0 = 50$. The CWT spectra of the signal y(t) and its components, $y_1(t)$ and $y_2(t)$ are depicted in Fig. 1.

We now proceed to decomposing the harmonic components of y(t) by the proposed method. In accordance with (11), as a first step we select the harmonic regions in the CWT spectrum of y(t) (cf. Fig. 1a) that contain the harmonics that we wish to separate. In this simple example only two harmonic regions need to be defined, each having time-varying boundaries in the frequency-time plane – cf. Fig. 2.

Applying the ICWT expression (14), separately to each of the selected harmonic regions we compute the "inverted" harmonic components to obtain $\tilde{y}_1(t)$ and $\tilde{y}_2(t)$, which yields the harmonic decomposition of the signal y(t). In addition, by applying numerical Hilbert transforms [24] to $\tilde{y}_1(t)$ and $\tilde{y}_2(t)$ we can numerically estimate the corresponding approximations for their frequencies, $\tilde{\Omega}_1(t)$ and $\tilde{\Omega}_2(t)$. In Fig. 3 we depict the comparisons between $\tilde{y}_k(t)$, $y_k(t)$ and the signal $y_k(t)$ that was identified using the WBEMD [8,9] method. In addition, we depict $\tilde{\Omega}_k(t)$, $\Omega_k(t)$ and the identified signal frequency $\Omega_k(t)$ by the WBEMD method, for k=1,2. These results show almost exact recovery of the two harmonic components of the original signal using the proposed ICWT, whereas WBEMD (and, in turn, EMD) fails. The inability of EMD-based techniques to separate $y_1(t)$ and $y_2(t)$ stems from the fact that the frequency ratio between harmonics is between 0.5 and 2, and also, since EMD-based methods perform the decomposition based on stationary (time-invariant) masking frequencies. Note that this example highlights the capacity of the method to decompose even nonstationary measured responses. This is confirmed further by the plot of Fig. 4 depicting the comparison between the original signal, y(t), and the reconstructed signal, $\tilde{y}(t) = \tilde{y}_1(t) + \tilde{y}_2(t)$. To quantify the discrepancy between the original and reconstructed signals, we computed the coefficient of determination as $R^2 = 0.999461$. It should be noted that even though the superposition of the extracted EMD components reconstruct the original signal, this does not guarantee that the extracted harmonics are necessarily meaningful.

Finally, we note that apart from the capacity of the proposed method to accurately decompose the harmonics of nonstationary signal, these results also show that the method is not affected by the issue of mode-mixing (which is a basic limitation of EMD) as the frequency ratio of the two harmonics of this signal varied between 0.5 and 2. This is further studied in the next section where the proposed method is applied to modal analysis of a linear system with two closely spaced modes.

3.2. Linear system of coupled oscillators – System identification and modal analysis

In this section we consider a linear 3 DOF system of coupled oscillators and show how the proposed inverse wavelet harmonic decomposition method is used to perform modal analysis of its dynamics. Due to a weak coupling stiffness this system has two closely spaced modes (or there is mode mixing), which makes purely data-driven system identification challenging to implement. The schematic of this system is shown in Fig. 5.

The governing equations of motion are given by,

$$\ddot{\mathbf{x}} + \mathbf{D}\dot{\mathbf{x}} + \mathbf{S}\mathbf{x} = \begin{bmatrix} 0 & 0 & \frac{f(t)}{m} \end{bmatrix}^{\mathrm{T}}, \mathbf{x}(0) = 0, \dot{\mathbf{x}}(0) = 0$$
(17)

where,

$$\mathbf{D} = \mathbf{M}^{-1}\mathbf{C} = \begin{bmatrix} \frac{1}{m} & 0 & 0 \\ 0 & \frac{2}{m} & 0 \\ 0 & 0 & \frac{1}{m} \end{bmatrix} \begin{bmatrix} c & 0 & 0 \\ 0 & c/2 & 0 \\ 0 & 0 & c \end{bmatrix} = \begin{bmatrix} \frac{c}{m} & 0 & 0 \\ 0 & \frac{c}{m} & 0 \\ 0 & 0 & \frac{c}{m} \end{bmatrix},$$

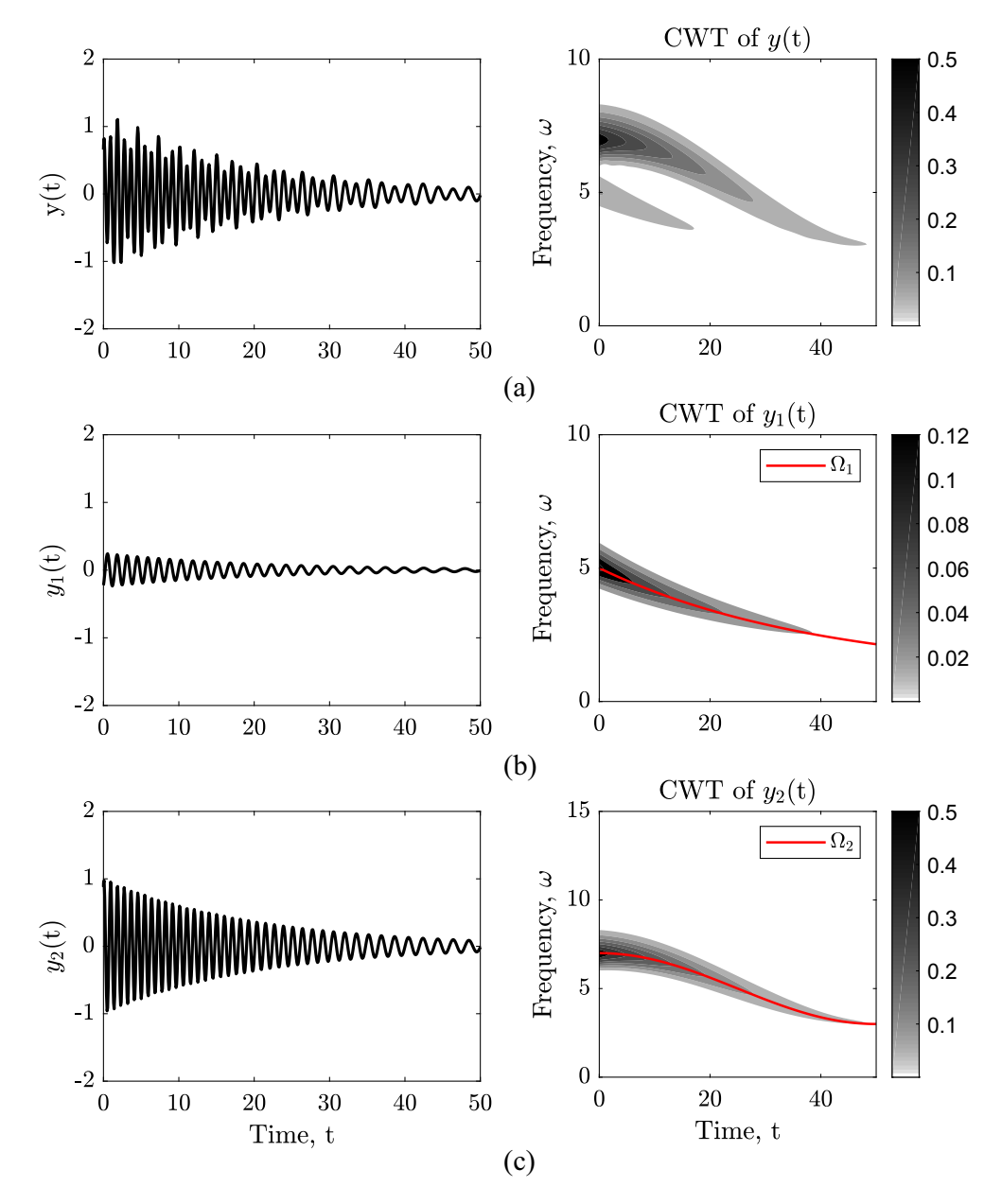


Fig. 1. Time series and respective CWT spectrum of (a) the signal y(t), (b) the harmonic component $y_1(t)$ and (c) the harmonic component $y_2(t)$; red curves are the exact component frequencies. (For interpretation of the references to colour in this figure legend, the reader is referred to the web version of this article.)

$$\mathbf{S} = \mathbf{M}^{-1} \mathbf{K} = \begin{bmatrix} \frac{1}{m} & 0 & 0 \\ 0 & \frac{2}{m} & 0 \\ 0 & 0 & \frac{1}{m} \end{bmatrix} \begin{bmatrix} 2k & -k & 0 \\ -k & 2k + \varepsilon k & -\varepsilon k \\ 0 & -\varepsilon k & k_3 + \varepsilon k \end{bmatrix} = \begin{bmatrix} \frac{2k}{m} & -\frac{k}{m} & 0 \\ -\frac{k}{m} & \frac{(2+\varepsilon)k}{m} & -\frac{\varepsilon k}{m} \\ 0 & -\frac{\varepsilon k}{m} & \frac{k_3 + \varepsilon k}{m} \end{bmatrix}$$

where **M**, **K** and **C** are the mass, stiffness and damping system matrices, respectively. In the specific application considered, we take $c/m = 0.1 \text{Nsm}^{-1} \text{kg}^{-1}$, $k/m = 100 \text{Nm}^{-1} \text{kg}^{-1}$, and $\varepsilon = 0.1$. In addition, by selecting $k_3/m = 100 \left(3 - \sqrt{3}\right)$, the frequency of the rightmost oscillator with response x_3 is equal to the frequency of the first mode of the two DOF subsystem composed of the oscillators with responses x_1, x_2 , obtained in the degenerate limit of $\varepsilon = 0$. This ensures that when ε is non-zero but small, the 3 DOF system, as a whole, possesses two closely spaced modes. Moreover, we select a transient excitation of the form,

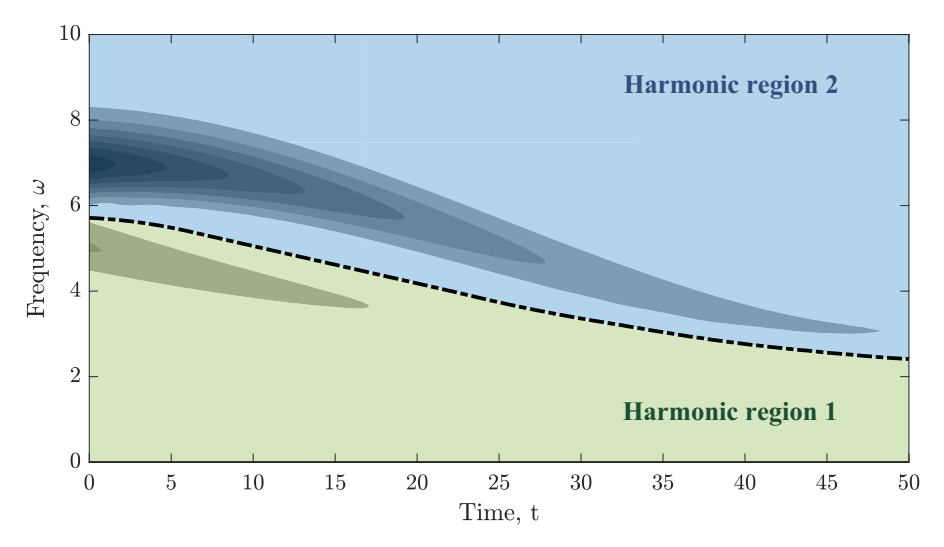


Fig. 2. Selected harmonic regions for the ICWT computations for the signal y(t), cf. eq. (15).

$$\frac{f(t)}{m} = \begin{cases} f_0 \sin\frac{\pi}{t_d} t & 0 \le t \le t_d \\ 0 & t_d \le t \end{cases},\tag{18}$$

with $f_0 = 10 \text{Nkg}^{-1}$. The responses of the oscillators of system (17) subjected to the transient forcing (18), is depicted in Fig. 6, together with their corresponding CWT spectra. Note that the two closely spaced modes result in a beat phenomenon between the two lower modes, which clearly appear in the wavelet spectra. This beat phenomenon introduce additional challenges in the harmonic decomposition exercise.

The three modes of the system were extracted by solving the corresponding eigenvalue problem for (17), yielding the following results,

$$\begin{split} &\left\{\widehat{\omega}_{1},\lambda_{1},\phi_{1}\right\} = \left\{11.2603,0.1,\left[0.6947,0.5086,0.5086\right]^{T}\right\}, \\ &\left\{\widehat{\omega}_{2},\lambda_{2},\phi_{2}\right\} = \left\{12.5858,0.1,\left[0.5234,0.2177,-0.8238\right]^{T}\right\} \\ &\left\{\widehat{\omega}_{3},\lambda_{3},\phi_{3}\right\} = \left\{22.7288,0.1,\left[0.3005,-0.9515,0.0652\right]^{T}\right\} \end{split}$$

where $\widehat{\omega}_i$, λ_i and φ_i denote the natural frequency, modal damping coefficient and mode shape of the i-th mode, respectively. We note that by design the first and the second modes of this system are closely spaced, and so mode mixing exists. Now, without assuming any prior knowledge of the system, except for the measured velocity time series, $\dot{x}_i(t)$, i=1,2,3

Now, without assuming any prior knowledge of the system, except for the measured velocity time series, $\dot{x}_i(t)$, i=1,2,3 and their corresponding CWT spectra, we apply the proposed inverse wavelet harmonic decomposition, with the purpose of performing modal analysis. We begin by selecting appropriate harmonic regions of the velocity wavelet spectra in the frequency-time domain, as shown in Fig. 7. Note that the boundary between the first and the second harmonic regions partitions the wavelet spectra of the beat phenomena, so the selection of the harmonic regions was dictated by our observations of the topologies of the CWT spectra. A tip for selecting the harmonic regions in the wavelet spectra of the responses of multiple points of a system (similar to this example) is to select the signal with the richest harmonic content in its wavelet spectrum, and then select its harmonic regions accordingly. Then use the same harmonic regions for the other of the responses. Since the harmonics represent the component dynamics of a system, their traces exist in all measured responses. This further illustrates the versatility of the proposed method.

Applying numerically the inverse CWT expression (14) to each of the three harmonic regions of Fig. 7, we derive the harmonic decompositions shown in Figs. 8-10. Each of these figures depicts the decomposed harmonic components $\dot{x}_i^{(j)}$, i,j=1,2,3, i.e., the j-th harmonic component of the measured velocity time series $\dot{x}_i(t)$. Due to the near-monochromatic nature of the extracted harmonics, their frequencies can be extracted by applying the numerical Hilbert transform. Considering the results, we notice that the amplitudes of the two lower-frequency decomposed harmonics $\dot{x}_i^{(1)}$ and $\dot{x}_i^{(2)}$, i=1,2,3, are modulated, rather than being exponentially decaying (as the third harmonic $\dot{x}_i^{(3)}$, i=1,2,3). Clearly, this is due to the closely spaced frequencies of the first and the second modes (harmonics), so the modulations are direct reflections of the aforementioned beat phenomena. It will be shown later, however, that the modulations do not affect the following modal analysis that is based on the identified decomposed harmonics.

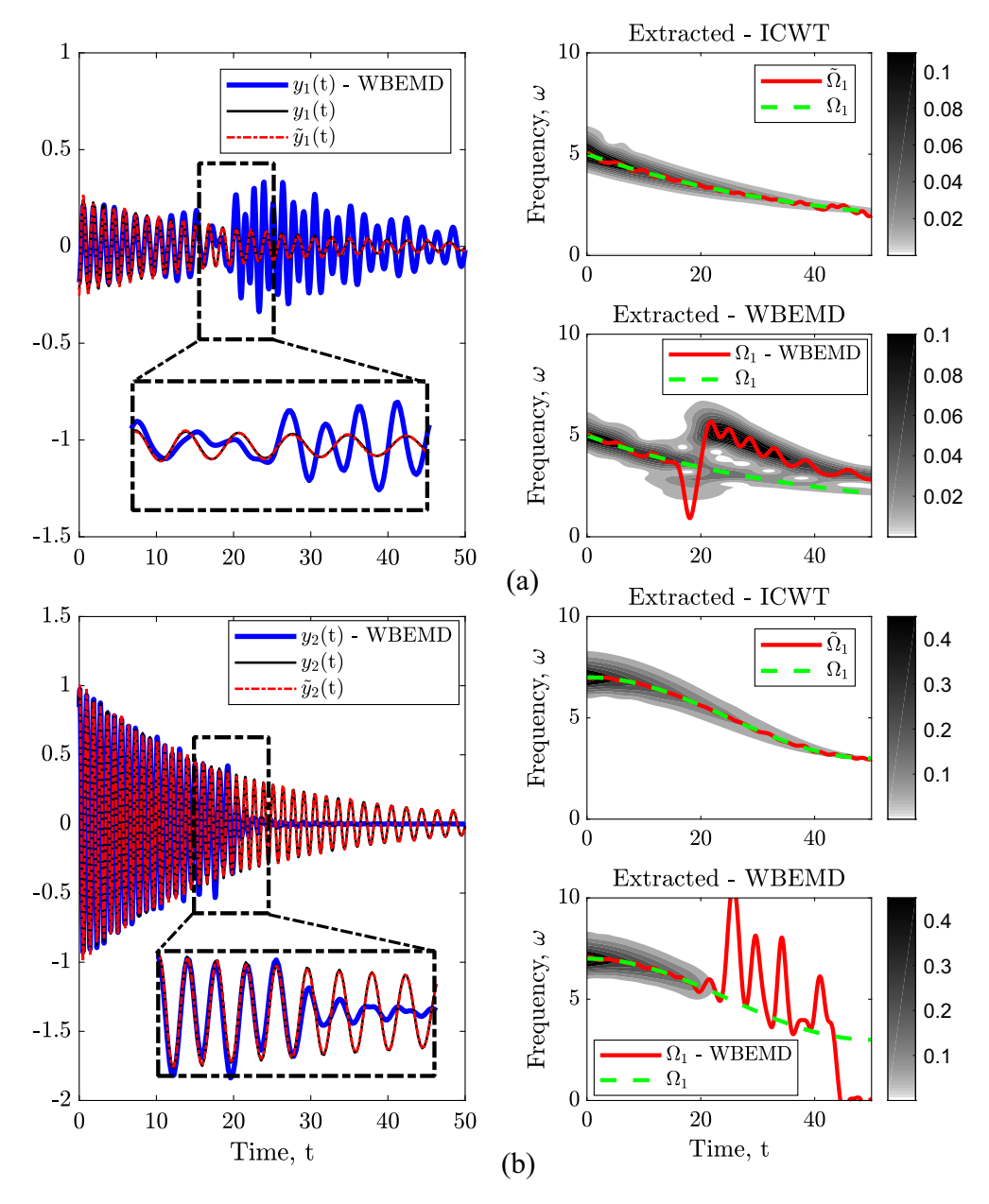


Fig. 3. Comparison between the time series, wavelet spectra and frequencies of the (a) first and (b) the second harmonic component of y(t), using the proposed ICWT and WBEMD methods with ground truth signal and values, $y_k(t)$ and Ω_k , k = 1, 2.

Disregarding the early and late portions of the decomposed signals (which are "polluted" by boundary effects [15]), i.e., the first and the last 10 s of the time series of the decomposed harmonics, $\dot{x}_i^{(j)}$, i,j=1,2,3, we obtain three different estimates for the j-th natural frequency by fixing j and applying the numerical Hilbert transform to the j-th decomposed harmonics $\dot{x}_1^{(j)}(t)$, $\dot{x}_2^{(j)}(t)$ and $\dot{x}_3^{(j)}(t)$. Then, the temporal average of the three resulting estimates $\overline{\omega}_{1j}(t)$, $\overline{\omega}_{2j}(t)$ and $\overline{\omega}_{3j}(t)$ provides the numerically estimated j-th natural frequency, $\overline{\omega}_{ij}$, of the system based on the i-th velocity time series $\dot{x}_i(t)$,

$$\overline{\widehat{\omega}}_{ij} = \frac{\int_{t_1}^{t_2} \overline{\omega}_{ij}(t)dt}{t_2 - t_1}, i, j = 1, 2, 3$$
(20)

where t_1 and t_2 represent the start and end boundaries defining the time interval of the measured signal that is considered in the system identification. Then, the final estimate for the j-th natural frequency is computed by $\overline{\widehat{\omega}}_j = \frac{1}{3} \sum_{i=1}^3 \overline{\widehat{\omega}}_{ij}, j = 1, 2, 3$.

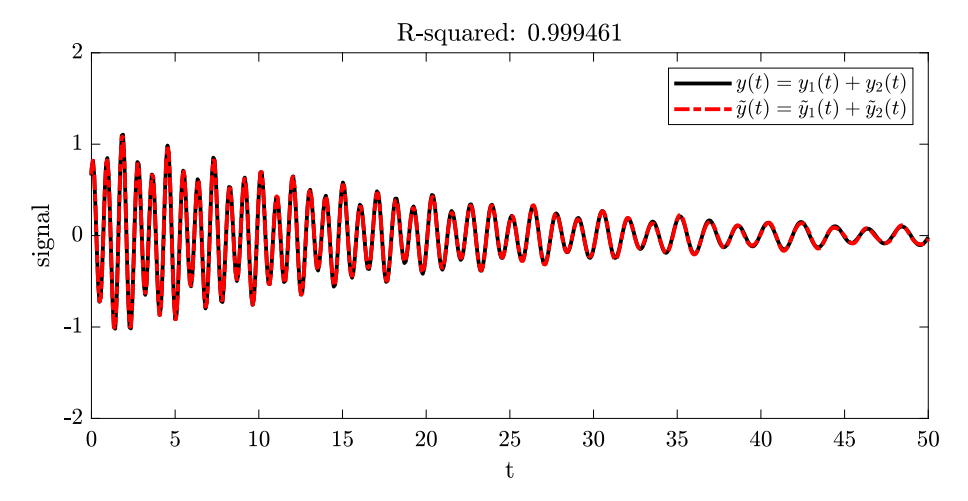


Fig. 4. Comparison between the original signal y(t), and the reconstructed y(t).

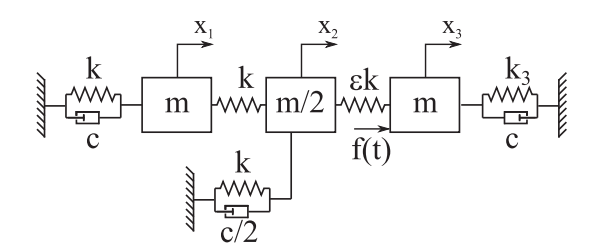


Fig. 5. The linear 3 DOF system with closely spaced modes.

Moreover, considering $\langle \dot{x}_i^{(j)} \rangle$, which denotes the amplitude of the decomposed harmonic $\dot{x}_i^{(j)}$, the j-th orthonormalized mode shape is estimated as follows,

$$\overline{\varphi}_{j} = \left[s_{1} \left\langle \dot{x}_{1}^{(j)} \right\rangle, s_{2} \left\langle \dot{x}_{2}^{(j)} \right\rangle, s_{3} \left\langle \dot{x}_{3}^{(j)} \right\rangle \right] / M_{j}, j = 1, 2, 3 \tag{21}$$

where

$$s_{k} \left\langle \dot{x}_{k}^{(j)} \right\rangle = \operatorname{sgn}\left[\frac{\dot{x}_{k}^{(j)}(t^{*})}{\dot{x}_{1}^{(j)}(t^{*})}\right], \dot{x}_{1}^{(j)}(t^{*}) \neq 0, k = 1, 2, 3, M_{j} = \left[\sum_{k=1}^{3} \left\langle \dot{x}_{k}^{(j)} \right\rangle\right]^{1/2}$$

$$(22)$$

where $sgn(\hat{A} \cdot)$ represents the signum function, and t^* is an arbitrarily selected time within the time interval where the system identification is performed.

Lastly, we obtain three different estimates for the j-th modal damping coefficient by fixing j and applying the concept of equivalent damping [25] for each of the j-th decomposed harmonics $\dot{x}_1^{(j)}(t), \dot{x}_2^{(j)}(t)$ and $\dot{x}_3^{(j)}(t)$. Then, taking the temporal average of the three resulting estimates $\hat{\lambda}_{1j}(t), \hat{\lambda}_{2j}(t)$ and $\hat{\lambda}_{3j}(t)$ provides the numerically estimated j-th modal damping coefficient, $\overline{\hat{\lambda}}_{ij}$, of the system based on the i-th velocity time series $\dot{x}_i(t)$,

$$\overline{\widehat{\lambda}}_{ij} = \frac{\int_{t_1}^{t_2} \widehat{\lambda}_{ij}(t) dt}{t_2 - t_1}, \widehat{\lambda}_{ij}(t) = -\frac{\frac{d}{dt} \left(\left\langle \dot{x}_i^{(j)}(t) \right\rangle^2 \right)}{\left\langle \dot{x}_i^{(j)}(t) \right\rangle^2}, i = 1, 2, 3$$
(23)

Then, the final estimate for the j-th modal constant coefficient is computed by $\overline{\lambda}_j = \frac{1}{3} \sum_{i=1}^3 \overline{\lambda}_{ij}^3$, j = 1, 2, 3. This completes the modal analysis based on the measured velocity time series.

In Table 1 we list the system identification results for the natural frequencies and compare them to the exact corresponding values. Note that the percentage relative error is computed as, $\left|\overline{\widehat{\omega}}_j - \widehat{\omega}_j\right|/\widehat{\omega}_j \times 100$ and is below 2.3%. However, due to the significantly small amplitude of $x_3(t)$ in the third mode (being a node for the third mode) from Fig. 10 we observe that the

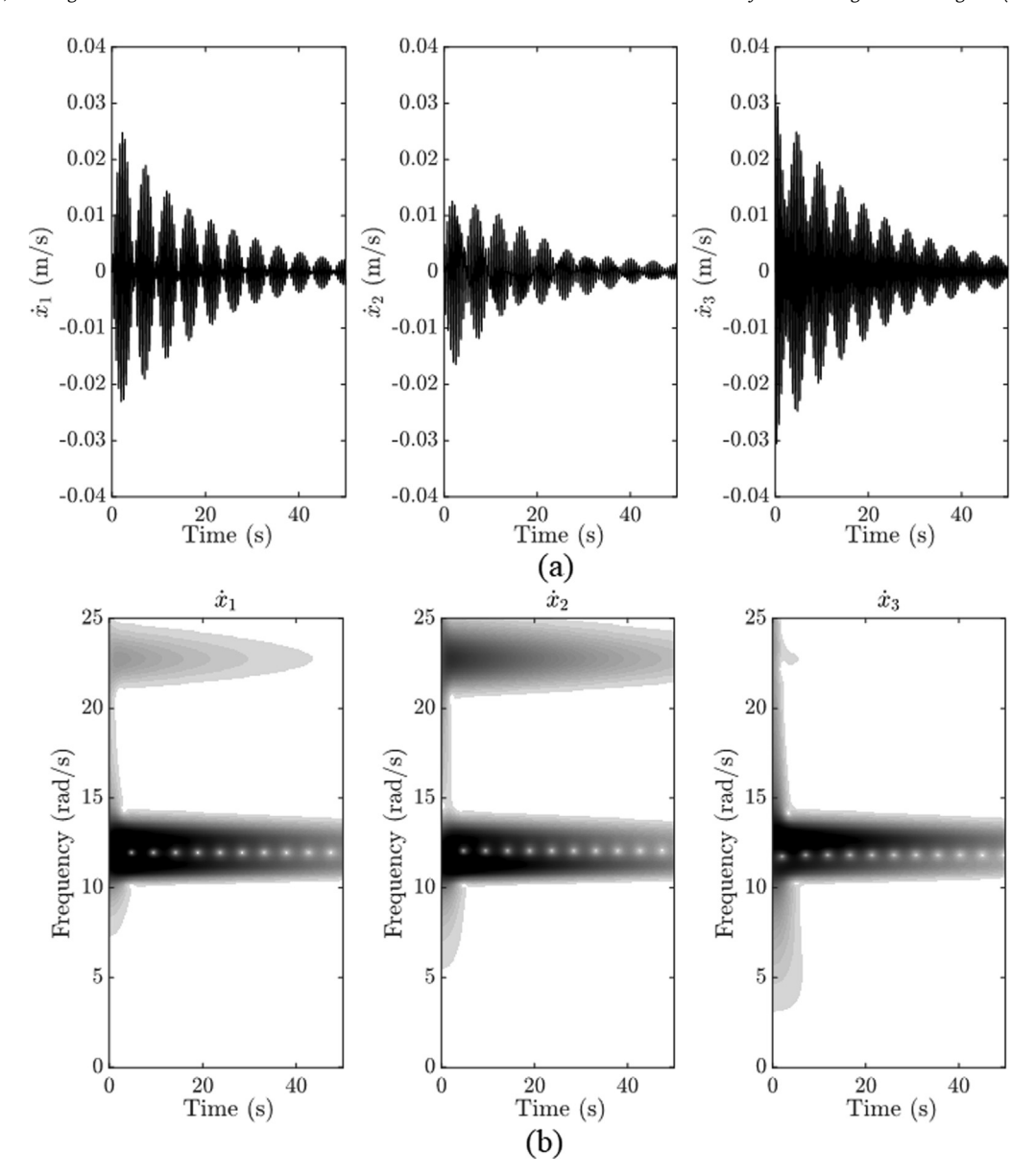


Fig. 6. Transient responses of system (17–18): (a) Velocity time series, and (b) respective CWTs.

third harmonic is the one most polluted by the boundary effects due to the numerical CWT; accordingly, if we exclude $\overline{\widehat{\omega}}_{33}$ (as an outlier) when estimating the third natural frequency, we obtain the estimate $\overline{\widehat{\omega}}_3 = 22.5596$ rad/s which would lead to the much smaller percentage relative error of 0.7444% for the third natural frequency. The identified and exact values of the modal damping coefficients are listed in Table 2. The j-th percentage relative error is computed by $|\widehat{\lambda}_j - \lambda_j|/\lambda_j \times 100$. Owing to the fact that the equivalent damping computation (23) results from an averaging operation, the slight modulations in the amplitude of the first and the second decomposed harmonics (cf. Figs. 8–10) are averaged out and the resulting final averaged estimates $\overline{\lambda}_j$ are close to their exact corresponding values, with the resulting percentage relative errors being less than 10%. However, if we exclude $\overline{\lambda}_{33}$ as outlier from the error computation (for the reason discussed above regarding the third harmonic), it would lead to the estimate $\overline{\lambda}_3 = 0.1001Nsm^{-1}kg^{-1}$, which would reduce the relative error to 0.1% in the third modal damping coefficient. These error estimates are satisfactory given that the two lower modes are closely spaced and the study is purely data-driven.

Lastly the identified and estimated mode shapes are listed in Table 3, and define the percentage relative error as $\|\overline{\varphi}_j - \varphi_j\|/\|\varphi_j\| \times 100$. From the listed values we conclude that the percentage relative error is below 1.5%. We observe

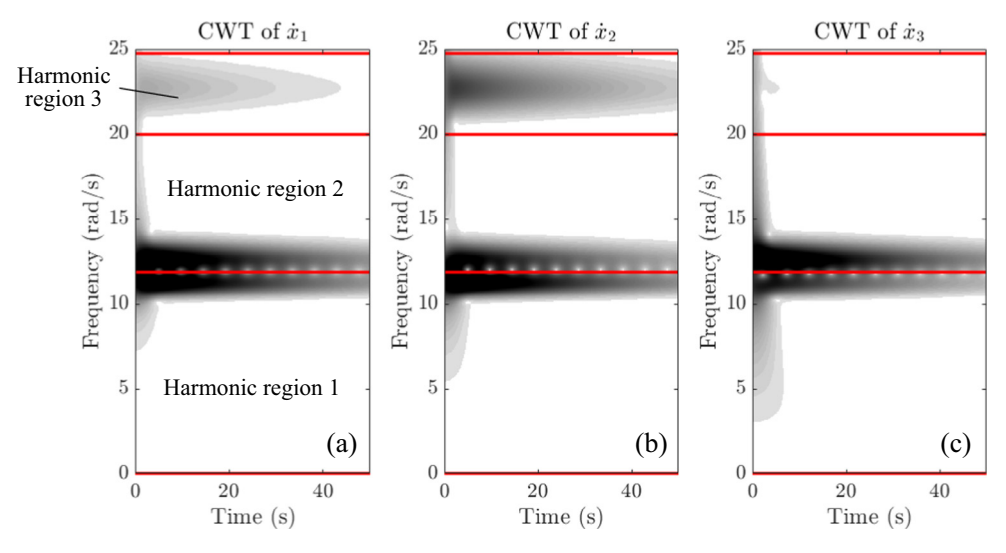


Fig. 7. The three selected harmonic regions in the CWT spectra of (a) $\dot{x}_1(t)$, (b) $\dot{x}_2(t)$ and (c) $\dot{x}_3(t)$; red lines represent the boundaries of the selected harmonic regions. (For interpretation of the references to colour in this figure legend, the reader is referred to the web version of this article.)

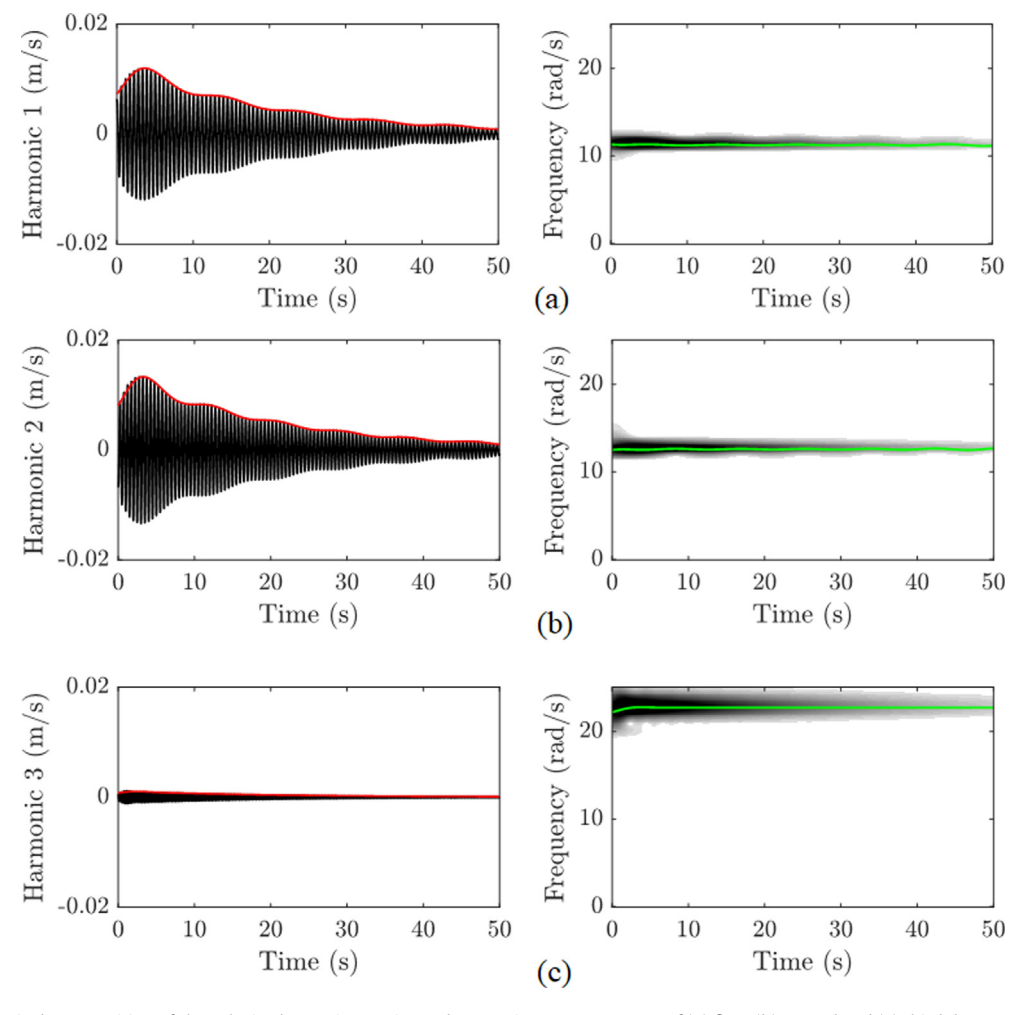


Fig. 8. Harmonic decomposition of the velocity $\dot{x}_1(t)$: Time series and respective CWT spectrum of (a) first, (b) second and (c) third decomposed harmonic; the amplitude modulations and frequencies of the decomposed harmonics are shown.

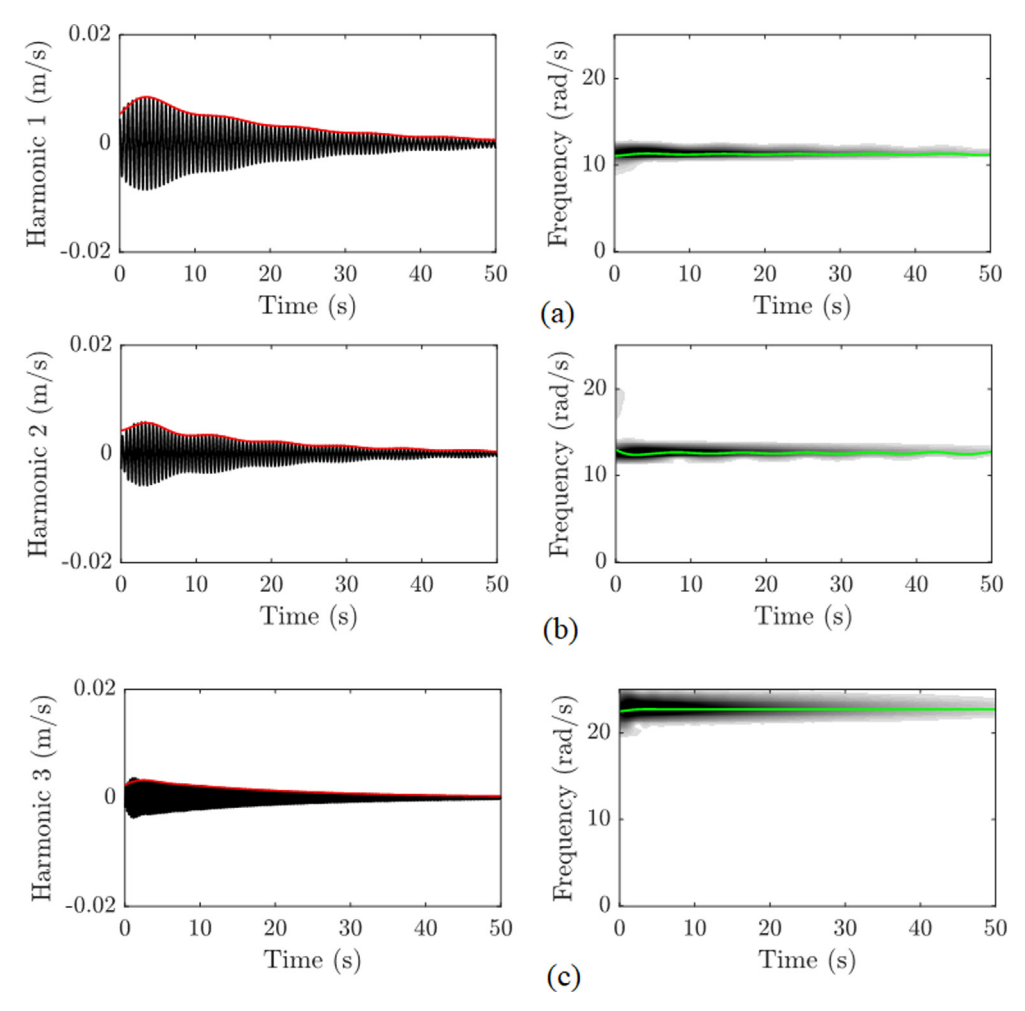


Fig. 9. Harmonic decomposition of the velocity $\dot{x}_2(t)$: Time series and respective CWT spectrum of (a) first, (b) second and (c) third decomposed harmonic; the amplitude modulations and frequencies of the decomposed harmonics are shown.

that the error for the third mode shape is higher compared to the other two modes. This is due to the fact that the magnitude of the third harmonic is very small in the response $x_3(t)$ compared to the magnitudes of the other two harmonics – cf. Fig. 10; this renders the identification of the third mode shape susceptible to the boundary effects in the CWT spectra and affects the numerical inverse wavelet transform as well. It must be noted that to compute the modal damping coefficients, one can consider the free decay (free response) of the system subjected to an impulse excitation. In most cases, the force applied to the system is known and using that information, user can determine when the free response of the system begins. However, in cases where the applied force is unknown, the time when the free response (free decay) of the system commences can be determined by examining its total energy and its corresponding decay rate. In this case, the free response of the system commences when the energy of the system begins to monotonically decay (for negative decay rates)

In conclusion, this example with coupled oscillators demonstrates the capacity of the proposed inverse wavelet-based method for modal analysis of measured data. Note that the achieved harmonic decomposition method is purely data driven, as it relies exclusively on the post-processing of measured time series. Also, the method allows the user to make intelligent selection of the topologies of the harmonic regions in order to achieve optimal decomposition (separation) of the dominant harmonic components; this aspect was particularly useful in this application as the measured data contained beat phenomena due to mode mixing. The application further illustrates the validity of the proposed method for system identification of general classes of single/multi-input – single/multi-output and time-varying / time-invariant linear systems. Moreover, the accuracy of the identified estimates, despite the existence of a pair of closely spaced modes, highlights the efficacy of the method as a valuable tool for performing modal analysis. In the next section we consider our last example with a strongly nonlinear oscillator, demonstrating the applicability of the proposed method for nonlinear systems as well.

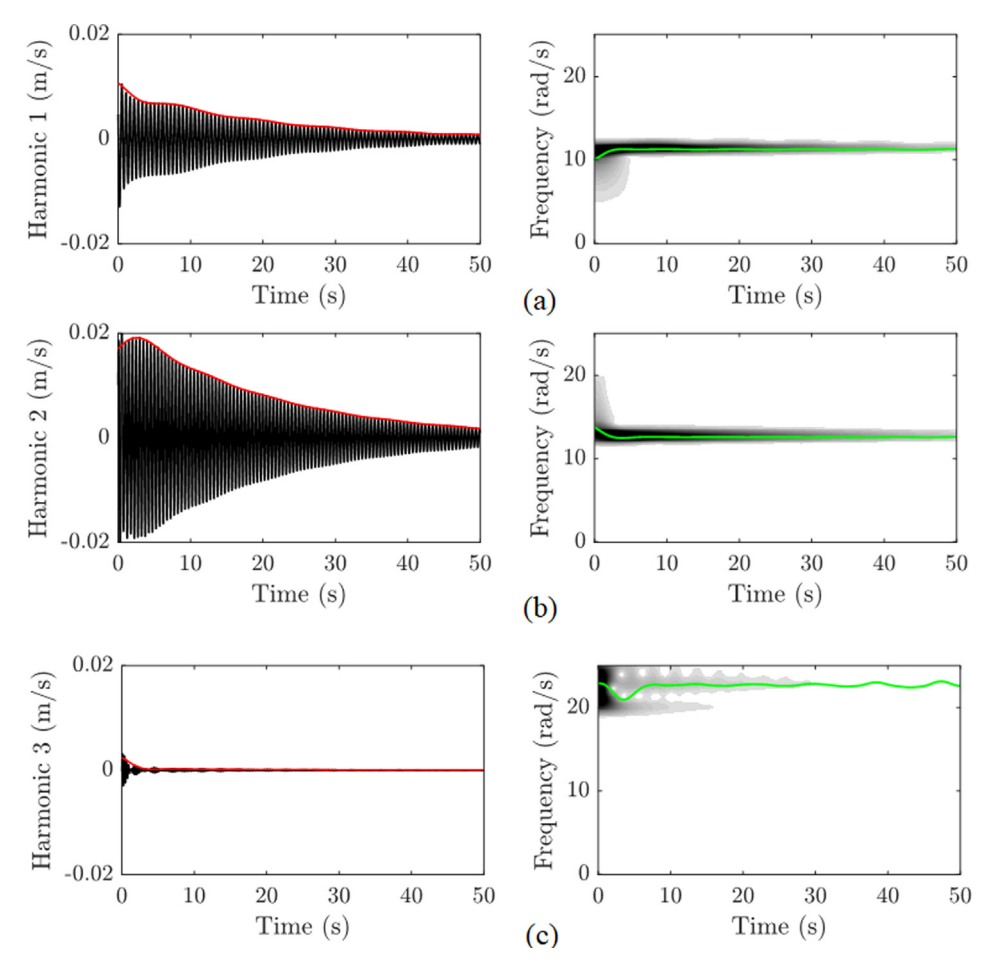


Fig. 10. Harmonic decomposition of the velocity $\dot{x}_3(t)$: Time series and respective CWT spectrum of (a) first, (b) second and (c) third decomposed harmonic; the amplitude modulations and frequencies of the decomposed harmonics are shown.

Table 1 Identified, averaged and exact natural frequencies of system (17).

	$\overline{\widehat{\omega}}_{1j}$	$\overline{\widehat{\omega}}_{2j}$	$\overline{\widehat{\omega}}_{3j}$	$\overline{\widehat{\omega}}_j = \frac{1}{3} \sum_{i=1}^3 \overline{\widehat{\omega}}_{ij}$	$\widehat{\omega}_{j}$	Relative error (%)
j = 1	11.4365	11.3729	11.3743	11.3946	11.2603	1.1921
j = 2	12.4384	12.3771	12.5634	12.4596	12.5858	1.0023
j = 3	22.4863	22.6329	21.5285	22.2159	22.7288	2.2565

Table 2 Identified, averaged and exact modal damping coefficients of system (17).

	$\overline{\widehat{\lambda}}_{1j}$	$\overline{\widehat{\lambda}}_{2j}$	$\overline{\widehat{\lambda}}_{3j}$	$\overline{\widehat{\lambda}}_j = \frac{1}{3} \sum_{i=1}^3 \overline{\widehat{\lambda}}_{ij}$	λ_j	Relative error (%)
j=1	0.1035	0.1027	0.0970	0.1011	0.1000	1.0617
j = 2	0.1109	0.1154	0.1024	0.1096	0.1000	9.5713
j = 3	0.1001	0.1001	0.0700	0.0900	0.1000	9.9514

3.3. Single DOF nonlinear oscillator - Energy scattering in the frequency domain

In this last application we will be examining the response of a single DOF oscillator with geometric stiffness and damping nonlinearities. By applying the introduced harmonic decomposition technique to analyze its transient response, we will decompose its dominant harmonics which, contrary to the previous example, are nonstationary. More importantly, based on this information we will quantify the energy captured by each harmonic, and, therefore, study the scattering of energy in the frequency domain due to the geometric nonlinearities.

Table 3 Identified and exact mode shapes of system (17).

Identified (\overline{arphi}_j) and exact $(arphi_j)$ mode shapes	Relative error (%)		
$\overline{\varphi}_1 = \left[0.6916, 0.5066, 0.5122\right]^T$	0.5243		
$\varphi_1 = [0.6947, 0.5086, 0.5086]^{\mathrm{T}}$			
$\overline{\varphi}_2 = [0.5251, 0.2195, -0.8218]^T$	0.3163		
$\varphi_2 = [0.5234, 0.2177, -0.8238]^{\mathrm{T}}$			
$\overline{\varphi}_3 = [0.3002, -0.9505, 0.0800]^T$	1.4820		
$\varphi_3 = [0.3005, -0.9515, 0.0652]^{\mathrm{T}}$			

The considered single-DOF oscillator is shown in Fig. 11. It consists of a mass m, attached to ground by a linear spring-viscous damper pair deforming in the direction of oscillation, and an inclined linear spring and damper pair situated with an initial angle ϕ_0 with respect to the vertical direction. An intriguing feature of this system is that *depending on angle* ϕ_0 *the nonlinear response can be hardening or hardening-softening*; in this section we will consider both of these cases. No external forcing is applied, and the response is due solely to the initial conditions. Even though this system is composed of linear elements, the geometric effects due to the deformation of the inclined spring-damper pair yield strong nonlinearities [21–23]. Assuming the oscillator deforms in the horizontal direction by x(t) and arbitrary initial conditions, the governing nonlinear equation of motion is given by,

$$m\ddot{x}(t) + d_{l}\dot{x}(t) + k_{l}x(t) + d_{i}\dot{x}(t) \left[\frac{y^{2}(t)}{L^{2} + y^{2}(t)}\right] + k_{i}y(t) \left[1 - \frac{Lsec\phi_{0}}{\sqrt{L^{2} + y^{2}(t)}}\right] = 0,$$

$$x(0) = X_0, \dot{x}(0) = V_0 \tag{24}$$

where $y(t) = x(t) + Ltan\phi_0$, and overdots denote differentiation with respect to time t. The dimensional equation (24) can be rewritten in non-dimensional form as.

$$u''(\tau) + \left(\lambda_l + \lambda_i \frac{\hat{y}^2(\tau)}{1 + \hat{y}^2(\tau)}\right) u'(\tau) + u(\tau) + \beta \hat{y}(\tau) \left(1 - \frac{\sec\phi_0}{\sqrt{1 + \hat{y}^2(\tau)}}\right) = 0,$$

$$u(0) = u_0, u'(0) = w_0 (25)$$

where we introduce the normalized time $\tau = t\sqrt{k_l/m}$, and $\lambda_{l,i} = d_{l,i}/\sqrt{k_lm}$, $\beta = k_i/k_l$, u = x/L, $\hat{y} = y/L$, and (.)' denotes differentiation with respect to τ .

Due to the nonlinearity the response of this system contains multiple harmonics, in contrast to an unforced linear single-DOF oscillator that responds with a single harmonic (at its natural frequency). Each of these harmonics captures a portion of the energy of the oscillator, resulting effectively in *nonlinear scattering of energy in the frequency domain*. We wish to apply the proposed method to quantify this nonlinear energy scattering. Accordingly, before discussing the response of (25), we provide a formulation that enables quantification of the contribution of each of the dominant harmonics of the nonlinear

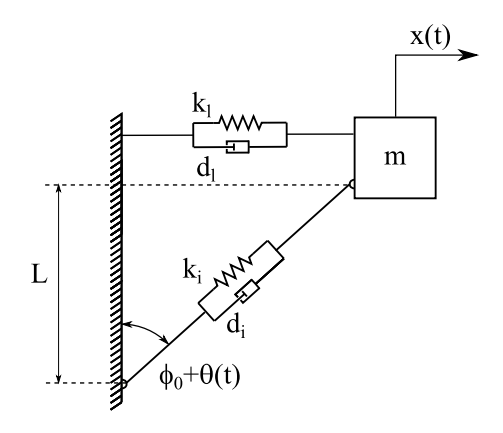


Fig. 11. System with inclined support yielding geometric stiffness and damping nonlinearities.

response to the energy of the oscillator. To achieve this, we assume that the velocity of the oscillator (25) consists of several harmonics, so we may express it in the following form,

$$u'(\tau) \equiv v(\tau) = \sum_{i=1}^{N} v_i(\tau) \tag{26}$$

where N is the number of (monochromatic) harmonics present in $v(\tau)$, and $v_i(\tau)$ represents the i-th harmonic in the velocity time series. Then, assuming that the time interval required for the response to decay nearly to zero is equal to T, we express the time-averaged energy of the signal $v(\tau)$ as follows:

$$\widetilde{K} = \lim_{T \to \infty} \frac{1}{2T} \int_{0}^{T} v^{2}(\tau) d\tau = \lim_{T \to \infty} \frac{1}{2T} \sum_{i=1}^{N} \int_{0}^{T} v_{i}^{2}(\tau) d\tau = \sum_{i=1}^{N} \widetilde{K}_{i}$$
(27)

In writing (27) we omitted the cross-product terms in the integrand, as it can be shown that all terms of the form $\int_0^T v_i(\tau)v_j(\tau)d\tau$ may be omitted for $i,j\in[1,\cdots,N], i\neq j$, provided that the amplitudes of $v_i(\tau)$ and $v_j(\tau)$ are slowly varying compared to their fast frequencies (which are the dominant harmonics); this is what happens typically in the decaying responses of lightly damped, single-DOF oscillators, as is the oscillator (25). Note that the first averaged expression in (27) has the form of averaged (normalized) kinetic energy. Therefore, we can directly express the percentage contribution of each harmonic to the instantaneous kinetic energy of the oscillator as:

$$R_i = \frac{\widetilde{K}_i}{\widetilde{K}} \times 100 \tag{28}$$

Although (28) has been derived as the *percentage kinetic energy* captured by the *i*-th harmonic component, as shown in the Appendix, for lightly damped, SDOF oscillators the ratio R_i is identical to the *percentage total energy* captured by the *i*-th harmonic. Note that all quantities in (27) and (28) are readily available when we apply the proposed ICWT-based method to harmonically decompose the velocity time series (as we did in the previous two examples). It follows that now we have the tools not only to decompose the dominant harmonics of the nonlinear response, but also to quantify the relative importance of each of the decomposed harmonics in terms of the portion of the total kinetic energy that it captures.

In the following study we consider two different configurations of the nonlinear oscillator of Fig. 11, to show the tunability of its transient dynamics to the initial geometry (i.e., the initial angle of inclination ϕ_0). In both cases considered we fix the system parameters to the values, $\beta=10$, $\lambda_i=0$ and $\lambda_l=0.025$. In case I we consider a zero initial angle of inclination, $\phi_0=0$, and initial conditions $u_0=0$, $w_0=10$, whereas in case II we consider the nonzero angle of inclination, $\phi_0=23^\circ$, and initial conditions $u_0=0$, $w_0=4$. We will show that the transient dynamics changes completely when ϕ_0 changes. In each case, we will apply the ICWT-based method to decompose the harmonics of the velocity response in the normalized frequency window [0, 10], and ignore higher-frequency harmonics since their contributions to the response are negligible. Then, based on these harmonic decompositions we will examine the percentage of instantaneous total energy captured by each identified harmonic through the relations (27) and (28). This will provide us with quantitative information on the scattering of energy in the frequency domain that is induced by the geometric nonlinearities of the system.

In Fig. 12 we present the velocity time series and the corresponding CWT spectrum for case I. Since this is the transient response of a nonlinear system, it possesses multiple harmonics, which are odd multiples of the fundamental harmonic; moreover, since the frequencies of all harmonics vary with time – as expected since due to the nonlinearity there is a nontrivial frequency-amplitude dependence – the harmonic components are nonstationary signals. What is even more interesting in the nonlinear oscillator of Fig. 11 is that, as explained in [21–23], due to the symmetry of the restoring stiffness force-displacement relationship for initial angle $\phi_0 = 0$, only the odd harmonics appear in the response of the system (cf. Fig. 12) and the stiffness nonlinearity is of the hardening type. This means that the frequencies of the harmonics decrease with decreasing energy. It follows that since we will be considering the dominant harmonics with nondimensional frequencies below 10, only the two lower harmonic components need to be considered in the ICWT-based harmonic decomposition method. Note, however, that these nonlinear features will change when the initial angle ϕ_0 is increased, as discussed below.

In Fig. 13 we show the two selected harmonic regions, with each containing a dominant lower harmonic component of the velocity time series of Fig. 12. Applying the proposed method to perform the ICWT operations to the two harmonic regions – through relation (14) – we compute the two lower decomposed harmonics of the velocity and their corresponding CWT spectra. These are depicted in Fig. 14. As in example 1 (Section 3.1), the results show the capacity of the proposed method to decompose nonstationary harmonic components.

After decomposing the lower dominant harmonics of the velocity time series, we apply relations (27) and (28) to estimate the percentages of total energy captured by each. Doing so for the normalized time interval from $\tau = 0$ to $\tau = 400$, the percentages of the energies associated with each of the lower two dominant harmonics are depicted in Fig. 15. Note that in that plot the dependent variable τ was replaced by the instantaneous total (normalized) energy at the same time instant, $E(\tau)$:

$$E(\tau) = \frac{1}{2}u^{2}(\tau) + \frac{1}{2}u^{2}(\tau) + \frac{1}{2}\beta \left[\sqrt{1 + (u(\tau) + \tan\phi_{0})^{2}} - \sec\phi_{0}\right]^{2},$$
(29)

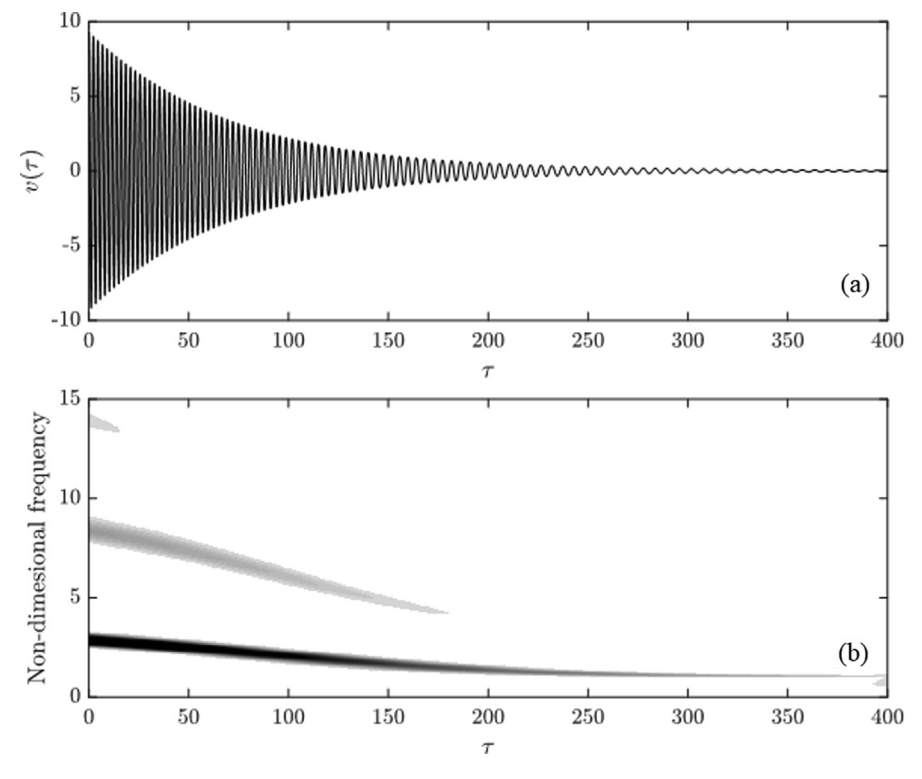


Fig. 12. Case I: (a) Velocity time series and (b) corresponding CWT spectrum; this is a case of hardening stiffness nonlinearity ($\phi_0 = 0$).

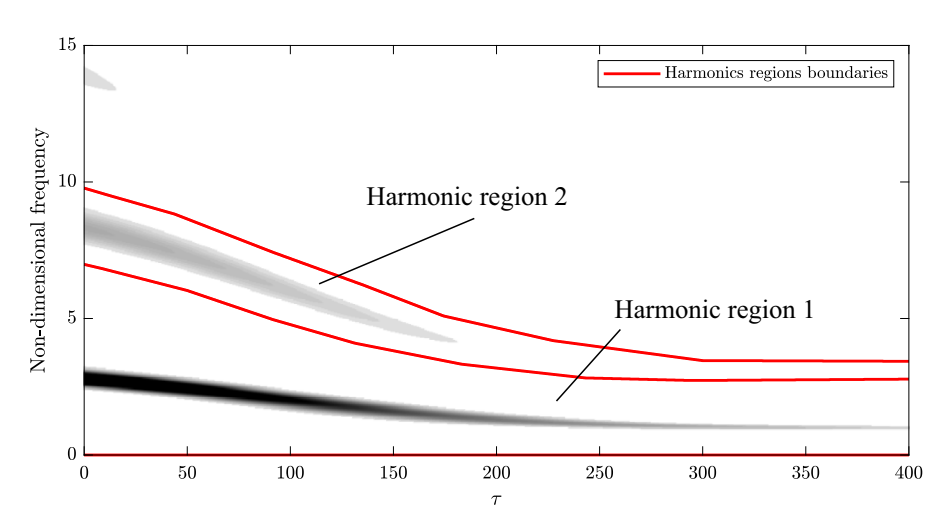


Fig. 13. The selected harmonic regions of the CWT spectrum for case I; the red curves represent the boundaries of the two harmonic regions. (For interpretation of the references to colour in this figure legend, the reader is referred to the web version of this article.)

this is permissible since, for the oscillator (25) the equivalence $\{\tau \leftrightarrow E(\tau)\}$ holds. The first observation is that the majority of the energy, above 99%, is captured by the first harmonic. Second, the results indicate that within a certain energy range, i.e., in the non-dimensional energy range [1–10], the second harmonic possesses its maximum percentage energy and this decreases for higher or lower energies. The fact that the second harmonic (which is entirely due to the geometric nonlinearities) possesses less percentage of energy at lower energy of the system is to be expected; indeed, as the energy of the system decreases, the effect of the nonlinearity decreases as well, and the higher harmonics playing a lesser role in the transient dynamics. It is interesting to note, however, that for this particular nonlinear oscillator, a similar effect occurs at high energy levels: As the energy of the system increases, the percentage of energy captured by the second harmonic component is found to decrease. This is explained when one notes that in the limit of high energies, i.e., large displacements, the expression for the restoring stiffness force attains a linear limit,

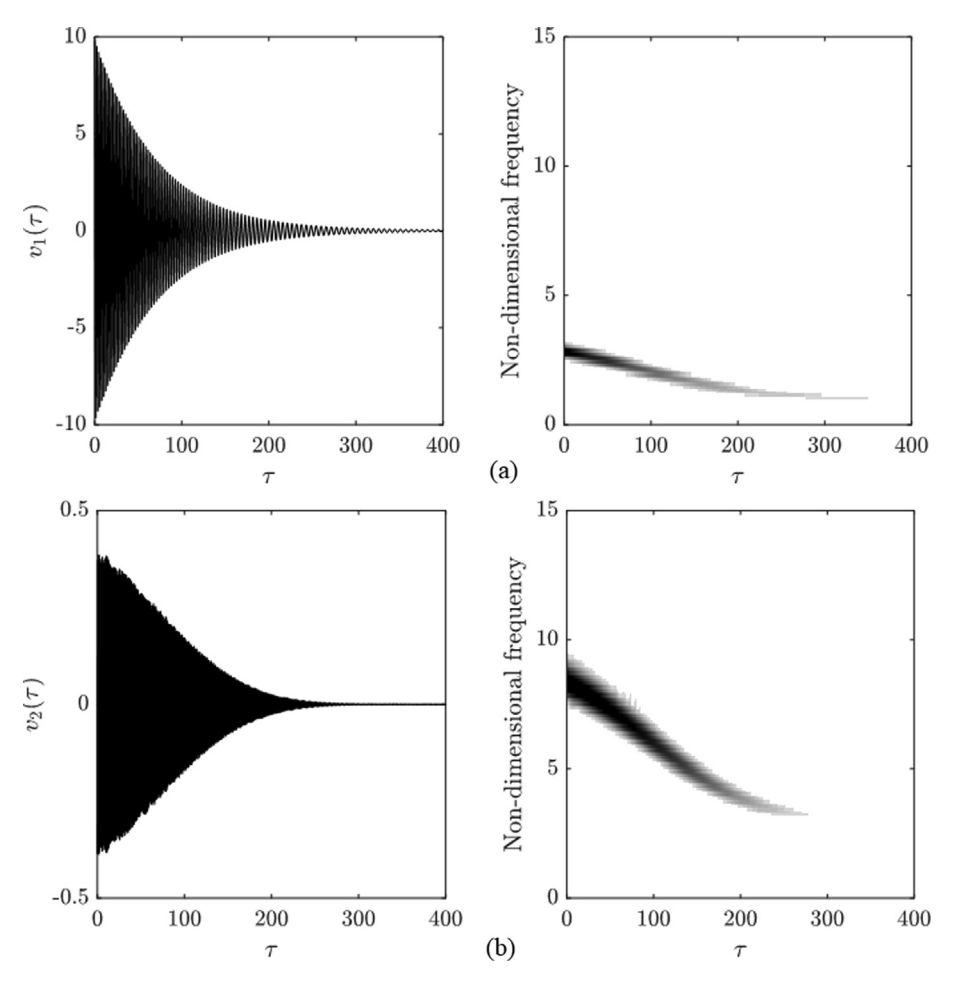


Fig. 14. Decomposed harmonic components for case I: Velocity time series and respective CWT spectra for (a) the first (lower frequency) harmonic, and (b) the second harmonic.

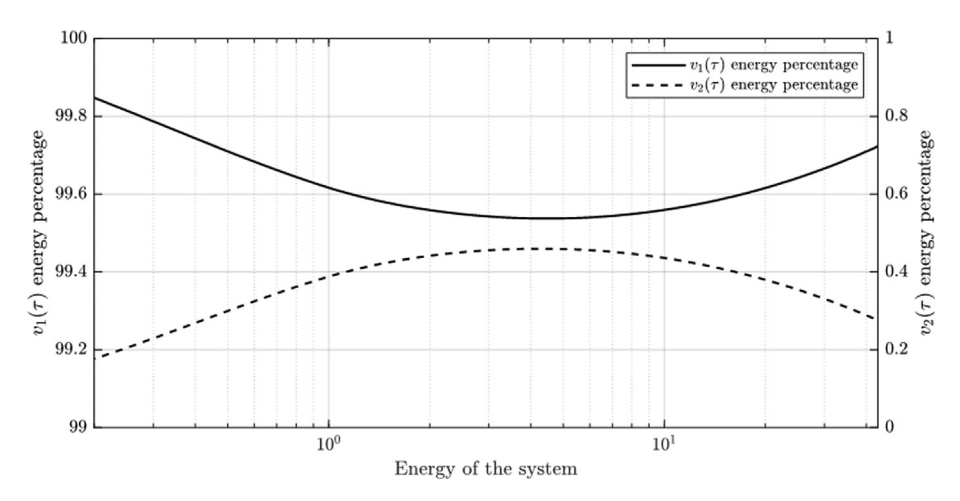


Fig. 15. Case I: Percentage of total energy captured by the first harmonic (solid curve – left vertical scale) and the second harmonic (dashed curve – right scale).

$$\lim_{u \to \infty} \left[u + \beta(u + \tan \phi_0) \left(1 - \frac{\sec \phi_0}{\sqrt{1 + (u + \tan \phi_0)^2}} \right) \right] = (1 + \beta)u(\tau)$$
(30)

which implies a linear limiting elastic restoring force and a linearization of the transient dynamics. In turn, this results in a decrease of the intensity of the second harmonic. Hence, the nonlinear oscillator of Fig. 11 tends to two linear systems in the limits of low or high energies, although these limiting linear systems differ. This explains the nonmonotonic behavior of the percentage of energy captured by the second harmonic component in Fig. 15. We conclude that the proposed method can be successfully applied to estimate the nonlinear energy scattering in the frequency domain.

Now we consider case II corresponding to the nontrivial initial angle of inclination $\phi_0=23^\circ$. The velocity response of the system for this case is shown in Fig. 16. Since ϕ_0 is nonzero, in this case the restoring stiffness force–displacement relationship is asymmetric about u=0; therefore, unlike the previous case with $\phi_0=0$ the nonlinear behavior of the system possesses both hardening and softening phases [16–18]. Indeed, from the wavelet transform spectrum of Fig. 16 we note that in the early, highly energetic phase of the dynamics the frequencies the dominant harmonics decrease with decreasing energy (i.e., as time increases), which indicates hardening nonlinear behavior; however, as time progresses these frequencies are shown to increase with decreasing energy, indicating softening nonlinear behavior. We conclude that, in contrast to case I where the nonlinear response was purely hardening, in case II there are hardening and softening phases in the transient dynamics. Moreover, from the results of Fig. 16 we deduce that, owing to the asymmetry of the stiffness restoring force, there are three dominant harmonic components below the non-dimensional frequency of 10, all of which need to be considered in the analysis. With these remarks we proceed to define 3 harmonic regions in the CWT spectrum of the velocity, each containing a dominant harmonic component, cf. Fig. 17. Then, by applying the ICWT inversion formula (14) to each selected harmonic region we decomposed the three leading harmonics, as shown in Fig. 18.

A noticeable observation in this case is that, unlike the first and the third harmonics whose amplitudes are monotonically decaying, the amplitude of the second harmonic initially increases and reaches its maximum at the approximately the same time when the nonlinearity switches its behavior from hardening to softening; after that point its amplitude decreases. This is in contrast to the monotonically decaying behavior of the two dominant harmonics in case I (cf. Fig. 14). This result is in agreement with the fact that the presence of the second harmonic is solely due to the softening nonlinear behavior of the system in this case, which, in turn, is directly related to the asymmetry of the restoring force–displacement relationship. Hence, the increase of the second harmonic is directly related to the "switch" of the nonlinear dynamics from hardening to softening behavior, so the plots of Fig. 18 corroborate the CWT spectrum of Fig. 16b. We deduce that in case II the second harmonic plays an important role in the transient dynamics, as it causes the switch between the hardening and softening nonlinear behavior.

After the harmonic decomposition of the velocity time series we proceed to apply the relations (27) and (28) to the identified harmonics in order to determine the percentages of energy captured by each. Fig. 19 depicts the percentage energy

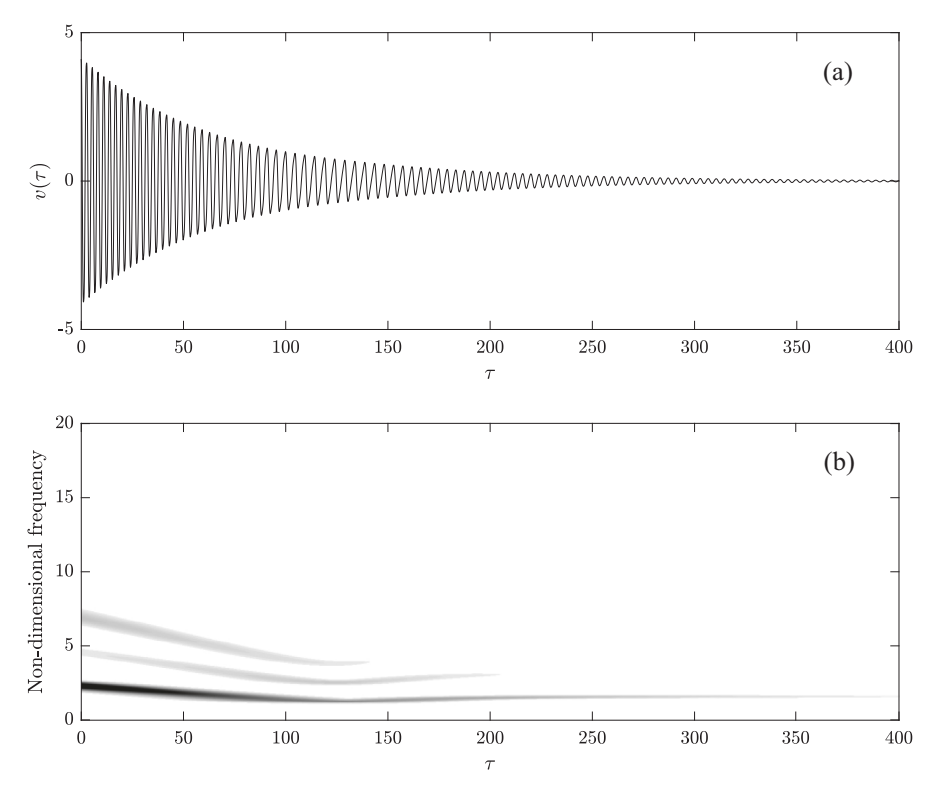


Fig. 16. Case II: (a) Velocity time series and (b) corresponding CWT spectrum; this is a case of hardening–softening stiffness nonlinearity $(\phi_0 = 23^\circ)$.

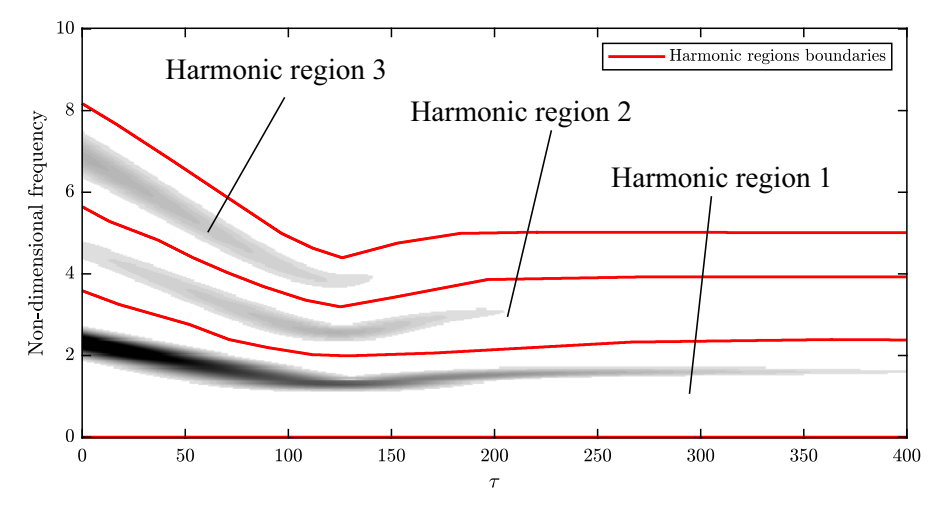


Fig. 17. The selected harmonic regions of the CWT spectrum for case II; the red curves represent the boundaries of the three harmonic regions.

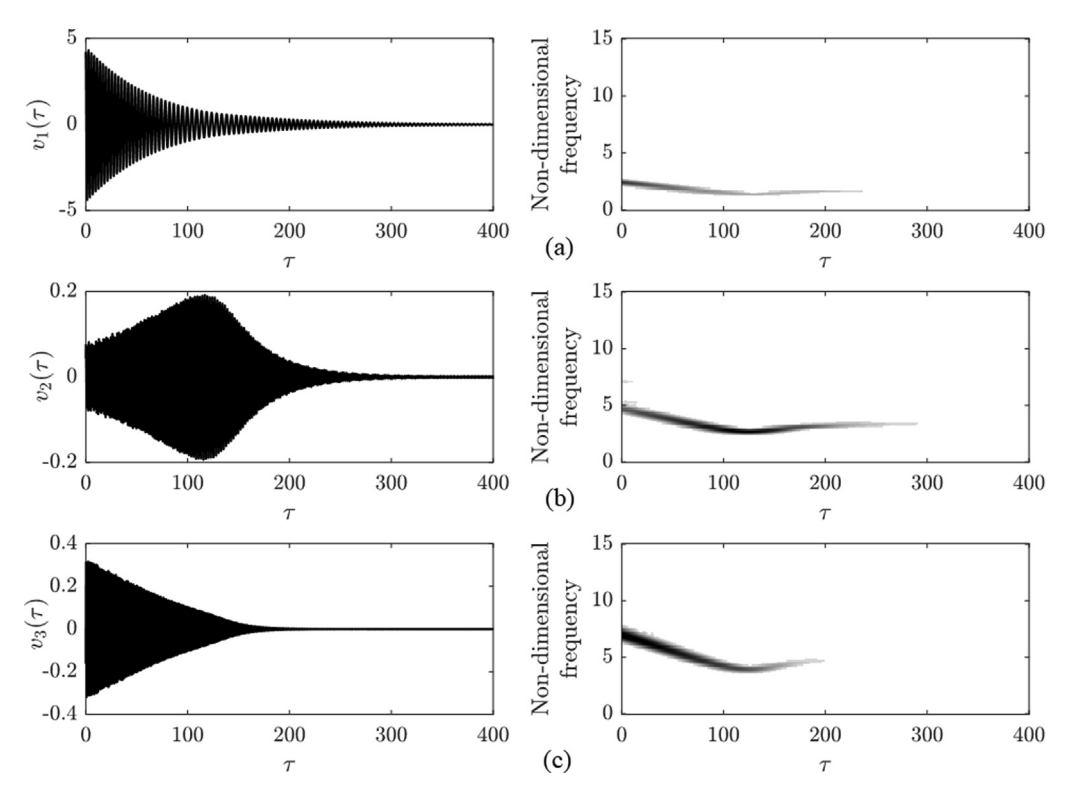


Fig. 18. Decomposed harmonic components for case II: Velocity time series and respective CWT spectra for (a) the first (lower frequency) harmonic, (b) the second harmonic, and (c) the third harmonic.

captured by each harmonic as function of the instantaneous energy of the system (as the energy decays from its initial value due to damping – so increasing time from left to right is equivalent to decreasing energy from right to left in that plot). Similar to what we observed in case I (cf. Fig. 15), the percentage energies captured by the second and third harmonics decrease as the energy of the system decreases and the system reaches a linear limiting behavior; as a result, the first harmonic captures nearly the entire energy in that regime. What is of importance, though, is that at the intermediate normalized energy level of 0.35 the percentage energy captured by the second harmonic increases significantly from less than 1% (at the high and low energy levels) to more than 4%, when at the same time the percentage energy captured by the first harmonic decreases from 98.5% to 95.5%. This intermediate energy level corresponds approximately to the time instant τ 111, which is when the stiffness nonlinearity of the system switches from hardening to softening (cf. Fig. 16b and 18). What this indicates is that the geometric nonlinearity of the system shown in Fig. 11 can be tuned by changing the initial angle of

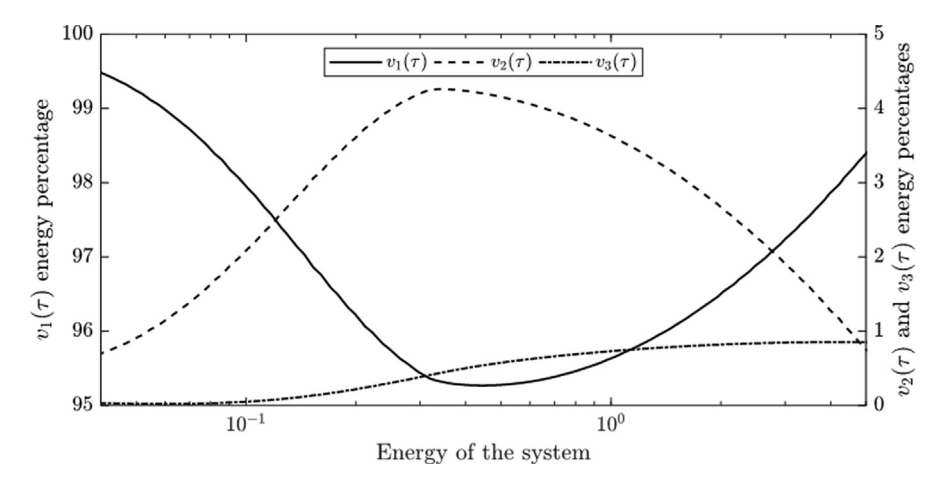


Fig. 19. Case II: Percentage of energy captured by the first harmonic (solid curve – left vertical scale), the second harmonic (dashed curve – right scale), and the third harmonic (dashed-dotted line – right scale).

inclination ϕ_0 so that the dynamics possesses combined hardening–softening type of nonlinearity; as shown by the results reported herein, this type of nonlinearity has enhanced capacity to scatter energy in the frequency domain.

4. Concluding remarks

A post-processing computational tool capable of decomposing different temporal (or spatial) scales in a signal is of great importance due to its applications in mechanical system identification, effective scale identification in dynamics and acoustics, signal processing, etc. In this work, we introduced a harmonic decomposition technique based on the numerical inverse continuous wavelet transform that overcomes the limitation of other current techniques, e.g., well-known limitations of EMD when mode mixing occurs in the measured data. The linear wavelet transformation transforms a signal from the time (or spatial) domain to the time–frequency (or space-wavenumber) domain. Because of this, the wavelet transform is capable of revealing important characteristics of signals that are not amenable to analysis by the classical Fourier transform, e.g., nonstationary nonlinear measured data.

Taking advantage of such benefits provided by the wavelet transform, we proposed a harmonic decomposition method based on the numerical inversion of the wavelet transform, and we successfully applied it to extract stationary and nonstationary frequency components of given signals. First, we introduced a basic formulation for computing the inverse continuous wavelet transform and expressed it in a way that is more suitable for efficient computational implementation. Then, we proposed the following algorithm to separate the scales (frequencies in our examples) in a measured signal in time domain: (i) Compute the wavelet transform of the signal; (ii) select a disjoint set of harmonic regions in the frequency-time domain of the computed wavelet spectrum, with each harmonic region containing a dominant harmonic frequency component that the user is interested to investigate; (iii) apply the numerical inverse wavelet transform formula to "invert" each harmonic region, thus recovering the corresponding dominant harmonic component in the time domain; and (iv) by superimposing all decomposed dominant harmonic components (nearly) reconstruct the original signal in the time domain. Following these steps, the user can extract the harmonic components of even nonstationary signals.

We demonstrated the efficacy of the proposed method with three examples of increasing complexity. First, we considered an artificial signal with prescribed stationary and nonstationary harmonic components and applied the inverse wavelet method to accurately recover them. Then, we applied the method to modal analysis of a system of linear coupled oscillators with a pair of closely spaced modes and were able to accurately identify the modal parameters despite the presence of mode mixing. Key to the success of modal analysis in this example was the versatility and flexibility of the method, which allowed us to carefully select the appropriate harmonic regions in the wavelet transform that allowed us to accurately decompose the two closely spaced modes.

In the last example we demonstrated applicability of the proposed method to nonlinear time series analysis, and showed that, apart from harmonically decomposing nonstationary harmonics, it can be used to quantify their relative importance, that is, the percentage of total energy of the system captured by each. Specifically, the method was applied to analyze the response of a lightly damped, single-DOF, geometrically nonlinear oscillator to investigate how the nonlinearity scatters energy in the frequency domain. Considering the dynamics in two different, hardening and hardening–softening regimes, we quantified the nonlinear scattering of energy from the first to higher harmonics. Moreover, we observed that the nonlinearity inflicts more intense energy scattering at the onset of switching behavior from hardening to softening nonlinearity.

The examples shown in this work demonstrate the broad applicability of the proposed method to general classes of dynamical and acoustical systems, linear and nonlinear, distributed and discrete, and time varying or time invariant.

Potential applications of this method are broad, e.g., linear and nonlinear system identification, study of nonlinear modal interactions and nonlinear modal energy exchanges, nonlinear energy scattering in the frequency domain, etc. Moreover, the proposed method can be directly applied to the analyze in detail the response of a nonlinear system, separate its fundamental harmonic from the rest of harmonics, and then obtain the frequency-amplitude relation not only for the fundamental but also for the other harmonics. Therefore, we envision application of the method in diverse applications across scales.

Declaration of Competing Interest

The authors declare that they have no known competing financial interests or personal relationships that could have appeared to influence the work reported in this paper.

Acknowledgment

This work was supported in part by National Science Foundation Grant No. CMMI-17-1727761. Any opinion, findings, and conclusions or recommendations expressed in this work are those of the authors and do not necessarily reflect the views of the National Science Foundation.

Appendix

For most mechanical systems, at a time instant where their kinetic energy reaches a maximum, the local maximum of the kinetic energy equals their total energy. Knowing this and the fact that the total energy of a damped system in a free response is monotonically decaying, we can approximate the total energy of a mechanical system by the envelope of the local maxima of its kinetic energy [20]. Now considering the free response of a lightly damped, single-DOF oscillator, where the decay of its total energy is a slow process governed by a time-scale that is much slower than the that of the "fast" oscillation at the fundamental harmonic inside the envelope, we may write,

$$\int_{t}^{t+T_p} E(s)ds = T_p \max_{T_p} \{K(t)\}$$
(A1)

where E(t) is the instantaneous total energy of the oscillator, T_p the period of the fundamental harmonic, and K(t) its instantaneous kinetic energy. Moreover, we can express the mean of K(t) over a period of the fundamental harmonic as follows:

$$\int_{t}^{t+T_{p}} K(s)ds = T_{p} \operatorname{mean}_{T_{p}} \{K(t)\}$$
(A2)

Combining (A1) and (A2), we obtain the following relation:

$$\int_{t}^{t+T_{p}} E(s)ds = \frac{\max_{T_{p}} \{K(t)\}}{\max_{T_{p}} \{K(t)\}} \int_{t}^{t+T_{p}} K(s)ds \tag{A3}$$

Expression (A3) relates the temporal integrals of the total and kinetic energies of a lightly damped, single-DOF oscillator. Combining (A3) with equations (26)–(28), we can compute the percentage of total energy allocated in each harmonic of the nonlinear response without explicitly computing the quantities $\max_{T_p} \{K(t)\}$ and $\max_{T_p} \{K(t)\}$, as these are constant factors in the numerator and denominator of expression (28) for R_i , so they cancel out.

References

- [1] E. Reynders, Arch. Comput. Methods Eng. 19 (2012) 51-124.
- [2] N.E. Huang, Z. Shen, S.R. Long, M.C. Wu, H.H. Shih, et al, Proceedings of the Royal Society of London, Series A: Math., Phys. Eng. Sci. 454 (1998) 903–995.
- [3] G. Rilling, P. Flandrin, P. Goncalves, On empirical mode decomposition and its algorithms. Presented at IEEE-EURASIP workshop on nonlinear signal and image processing, 2003.
- [4] H. Chen, M. Kurt, Y.S. Lee, D.M. McFarland, L.A. Bergman, A.F. Vakakis, Mech. Syst. Sig. Process. 46 (2014) 91–113.
- [5] M. Eriten, M. Kurt, G. Luo, D. Michael McFarland, L.A. Bergman, A.F. Vakakis, Mech. Syst. Sig. Process. 39 (2013) 245–264.
- [6] M. Kurt, H. Chen, Y.S. Lee, D.M. McFarland, L.A. Bergman, A.F. Vakakis, Arch. Appl. Mech. 82 (2012) 1461–1479.
- [7] M. Kurt, M. Eriten, D.M. McFarland, L.A. Bergman, A.F. Vakakis, J. Sound Vib. 333 (2014) 2054–2072.
- [8] K.J. Moore, M. Kurt, M. Eriten, D.M. McFarland, L.A. Bergman, A.F. Vakakis, Mech. Syst. Sig. Process. 99 (2018) 14–29.
- [9] K.J. Moore, M. Kurt, M. Eriten, D.M. McFarland, L.A. Bergman, A.F. Vakakis, Nonlinear Dyn. 93 (2018) 1559-1577.
- [10] S. Qin, Q. Wang, J. Kang, Adv. Mater. Sci. Eng. 2015 (2015) 945862.
- [11] A. Sadhu, J. Vib. Control 23 (2017) 2727–2741.
- [12] J. Allen, IEEE Trans. Acoust. Speech, Signal Process. 25 (1977) 235–238.
- [13] J.B. Allen, L.R. Rabiner, Proc. IEEE 65 (1977) 1558-1564.
- [14] L. Rabiner, J. Allen, IEEE Trans. Acoust. Speech, Signal Process. 27 (1979) 182–192.
- [15] P.S. Addison, The Illustrated Wavelet Transform Handbook: Introductory Theory and Applications in Science, Engineering, Medicine and Finance, Second Edition., CRC Press, 2017.
- [16] M. Boltežar, J. Slavič, Mech. Syst. Sig. Process. 18 (2004) 1065-1076.
- [17] C.S. Huang, W.C. Su, Mech. Syst. Sig. Process. 21 (2007) 1642–1664.
- [18] S. Wang, W. Zhao, G. Zhang, H. Xu, Y. Du, Mech. Syst. Sig. Process. 147 (2021) 107122.

- S. Quqa, L. Landi, D.P. Paolo, Mech. Syst. Sig. Process. 142 (2020) 106750.
 S. Quqa, L. Landi, D.P. Paolo, Mech. Syst. Sig. Process. 148 (2021) 107136.
 Y. Liu, A. Mojahed, L.A. Bergman, A.F. Vakakis, Nonlinear Dyn. 96 (2019) 1819–1845.
 A. Mojahed, L.A. Bergman, A.F. Vakakis, Proc. Inst. Mech. Eng., Part C: J. Mech. Eng. Sci. (2020) 1–20.
 A. Mojahed, K. Moore, L.A. Bergman, A.F. Vakakis, Int. J. Non Linear Mech. 107 (2018) 94–111.
 M. Feldman, Hilbert Transform Applications in Mechanical Vibration, Wiley, 2011.
 T.P. Sapsis, D. Dane Quinn, A.F. Vakakis, L.A. Bergman, J. Vib. Acoust. 134 (2012).